Journal of Power Sources 196 (2011) 7627–7638

Contents lists available at ScienceDirect

Journal of Power Sources

journal homepage: www.elsevier.com/locate/jpowsour

The effect of Mn on the oxidation behavior and electrical conductivity of Fe–17Cr alloys in solid oxide fuel cell cathode atmosphere

Bin Hua, Yonghong Kong, Wenying Zhang, Jian Pu*, Bo Chi, Li Jian

School of Materials Science and Engineering, State Key Laboratory of Material Processing and Die & Mould Technology, Huazhong University of Science & Technology, Wuhan, Hubei 430074, PR China

ARTICLE INFO

Article history:
Received 22 March 2011
Received in revised form 3 May 2011
Accepted 6 May 2011
Available online 17 May 2011

Keywords:
Solid oxide fuel cell
Metallic interconnect
Fe–Cr alloy
Oxidation kinetics
Area specific resistance

ABSTRACT

Four Fe–17Cr alloys with various Mn contents between 0.0 and 3.0 wt.% are prepared for investigation of the effect of Mn content on the oxidation behavior and electrical conductivity of the Fe–Cr alloys for the application of metallic interconnects in solid oxide fuel cells (SOFCs). During the initial oxidation stage (within 1 min) at 750 °C in air, Cr is preferentially oxidized to form a layer of Cr_2O_3 type oxide in all the alloys, regardless the Mn content, with similar oxidation rate and oxide morphology. The subsequent oxidation of the Mn containing alloys is accelerated caused by the fast outward diffusion of Mn ions across the Cr_2O_3 type oxide layer to form Mn-rich $(Mn, Cr)_3O_4$ and Mn_2O_3 oxides on the top. After 700 h oxidation a multi-layered oxide scale is observed in the Mn containing alloys, which corresponds to a multi-stage oxidation kinetics in the alloys containing 0.5 and 1.0 wt.% of Mn. The oxidation rate and ASR of the oxide scale increase with the Mn content in the alloy changes from 0.0 to 3.0 wt.%. For the application of metallic interconnects in SOFCs, Mn-free Fe–17Cr alloy with conducting Cr free spinel coatings is preferred.

1. Introduction

The interconnect is a critical stack component of solid oxide fuel cells (SOFCs). As the reduction of SOFC operating temperature into an intermediate temperature range of 600–800 °C, some metallic alloys have an opportunity to replace the conventional $LaCrO_3$ based ceramic materials as SOFC interconnects with advantages of high electronic and thermal conductivities, low material cost and easy fabrication. During the period of operation at a temperature between 600 and 800 °C with exposure to the fuel and oxidant atmospheres, an oxide scale is inevitably formed on the surface of the alloys, increasing the electrical resistance of the interconnect. In consideration of oxidation resistance, electrical conductivity and thermal expansion behavior, Cr_2O_3-forming ferritic Fe–Cr alloys are preferred for the interconnect application as Cr_2O_3 scale has an attractive balance of relatively low oxide growth rate and acceptably high electrical conductivity, compared to those form Al_2O_3 or SiO_2 scale [1–9]. Nevertheless, these alloys are still facing a serious challenge of insufficient oxidation resistance in a long-term SOFC operation; the thermally grown oxide scale upon SOFC operation will gradually increase the electrical resistance of the interconnect to an unacceptable level during the expected service lifetime of SOFCs even at the reduced temperatures [10–12].

The presence of Mn in alloys with Mn content below 1 wt.% leads to the formation of a double-layered oxide scale with $(Mn, Cr)_3O_4$ on top of Cr_2O_3, which is expected to improve the electrical conductivity of the scale and suppress the Cr evaporation as $(Mn, Cr)_3O_4$ possesses higher electrical conductivity and lower evaporation pressure than that of Cr_2O_3 [13–15]. Multi-stage oxidation kinetics, each obeying Wagner's parabolic law, was observed in SUS 430 and Haynes 230 alloys with a low Mn content [16,17], which can be attributed to faster diffusion of Mn ions in Cr_2O_3 than that of Cr ions and Mn deficiency and recovery in the substrate adjacent to the alloy/oxide scale interface [18–20]. However, the oxidation behavior and scale microstructure are sensitive to the Mn content in alloys. With further increase of Mn content, Mn-rich oxides, such as Mn_2O_3 and Mn_3O_4, form on the outermost surface of Fe–Cr alloys, resulting in a higher oxidation rate and oxide scale spallation, as reported by Stott et al. [21] and Marasco and Young [22].

In order to understand the effect of Mn on the oxidation resistance and electrical conductivity of Fe–Cr alloys for the application of SOFC interconnects, it is also necessary to investigate the early stage oxidation behavior, other than the long term one. Crouch and Scully [23] indicated that the presence of approximately 0.7% Mn in a commercial Fe–13Cr alloy results in preferential formation of a nonprotective Mn–Cr spinel in a controlled H_2–H_2O atmosphere at 800 °C during the early stage of oxidation. And with SUS 430

* Corresponding author. Tel.: +86 27 87557694; fax: +86 27 87558142.
E-mail address: pujian@hust.edu.cn (J. Pu).

0378-7753/$ – see front matter © 2011 Elsevier B.V. All rights reserved.
doi:10.1016/j.jpowsour.2011.05.007

Table 1
Chemical composition of prepared Fe–Cr–*x*Mn alloys (wt.%).

Alloy	Mn	Cr	C	S	P	Si	Fe
Fe–Cr–0.0Mn	<0.10	16.87	0.001	0.007	0.0100	0.049	Bal.
Fe–Cr–0.5Mn	0.52	16.80	0.001	0.008	0.0096	0.049	Bal.
Fe–Cr–1.0Mn	0.99	16.76	0.001	0.006	0.0098	0.043	Bal.
Fe–Cr–3.0Mn	2.84	16.90	0.002	0.008	0.0088	0.036	Bal.

alloys containing various contents of Mn (0.1–0.9 wt.%) oxidized at 1000 °C in 0.165 atm O_2-N_2 atmosphere, Saeki et al. [24] found that corundum type oxide forms within first 30 s followed by formation of spinel type oxide nucleated from the pre-existing corundum oxides. In the present study, a series of Fe–Cr alloys with different Mn contents were studied by oxidation at 750 °C in air for different durations of time. The effect of Mn content on the oxidation behavior of the Fe–Cr alloys, such as oxide nucleation and growth, oxide phase and morphology, and electrical conductivity of the oxide scale, were characterized.

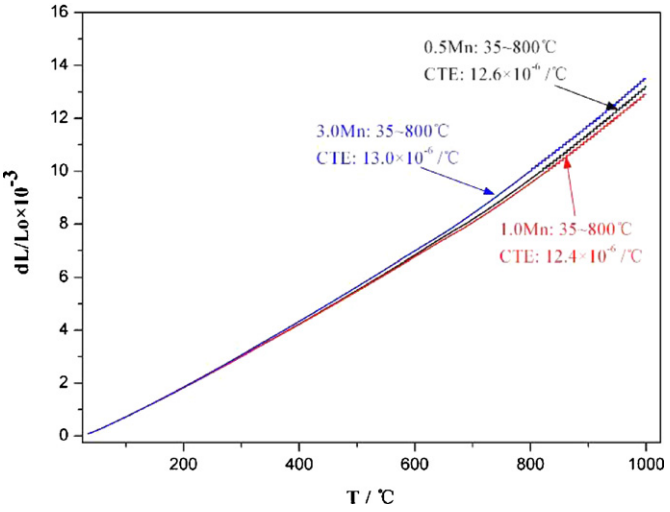

Fig. 1. Thermal expansion of the Fe–Cr–*x*Mn alloys as a function of temperature.

2. Experiment

The designed Fe–Cr based alloys with different amounts of Mn (Mn = 0.0, 0.5, 1.0 and 3.0 wt.%) were prepared with high-purity elemental materials by arc melting in vacuum. The homogenized ingot was processed into 1 mm thick sheets by forging, hot rolling and cold rolling, followed by conventional heat treatment. The chemical composition of the alloys was analyzed as listed in Table 1. Their coefficient of thermal expansion (CTE) was measured by a thermal dilatometer of DIL 402C (NETZSCH) as shown in Fig. 1. The CTE slightly increases with Mn addition from 12.4×10^{-6} to $13.0 \times 10^{-6}\,K^{-1}$ in the temperature range of 35 and 800 °C and is well matched to that of SOFC cell components (typically in the range of $10–13 \times 10^{-6}\,K^{-1}$). Rectangular coupons for oxidation evaluation with a dimension of 25 mm × 25 mm × 1 mm were cut from the heat treated alloy sheet by using an electrical discharge machine, and the coupon surfaces were ground with SiC papers up to 2000-grit, followed by mechanically polish. They were solvent cleaned ultrasonically and dried prior to oxidation.

Isothermal oxidation was performed at 750 °C in a furnace with stagnant air. Coupons for initial oxidation evaluation (within 50 h, typically within 10 min) were directly put into the furnace at 750 °C; and those for long-term oxidation (up to 700 h) were heated

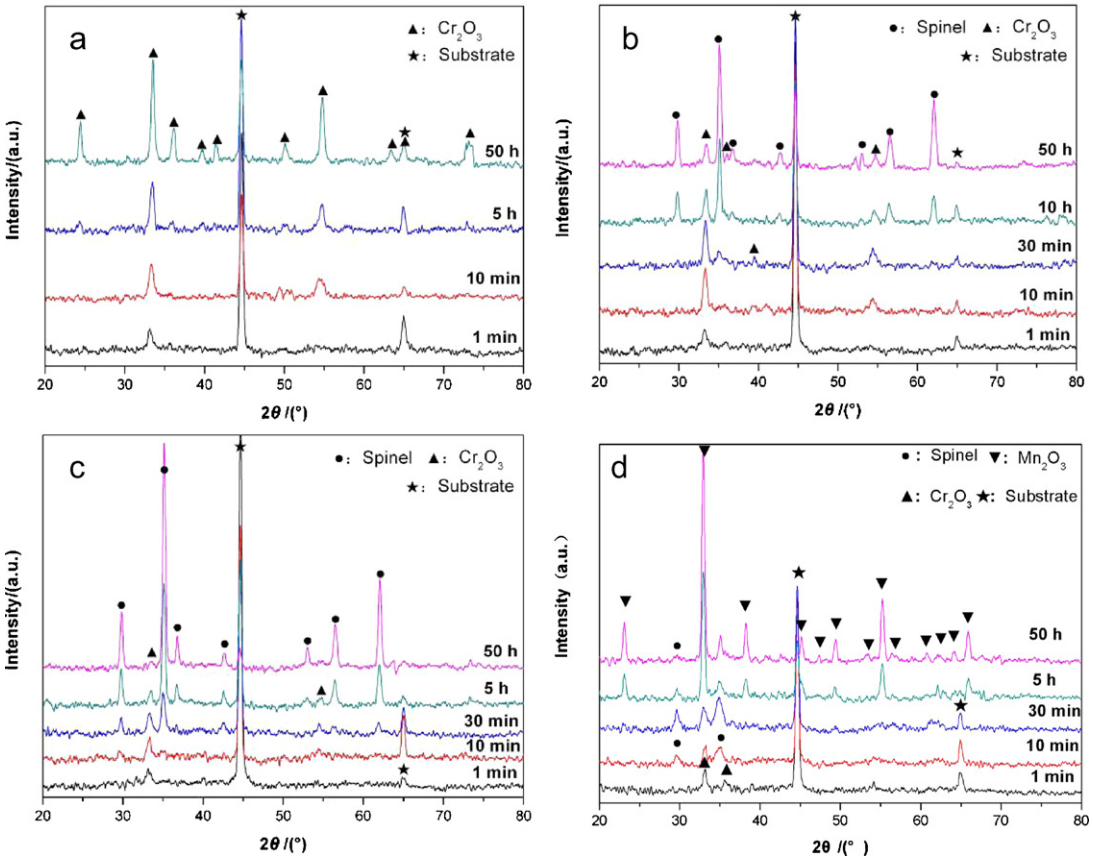

Fig. 2. XRD patterns of the Fe–Cr–*x*Mn alloys oxidized at 750 °C in air up to 50 h: (a) 0.0Mn; (b) 0.5Mn; (c) 1.0Mn; (d) 3.0Mn.

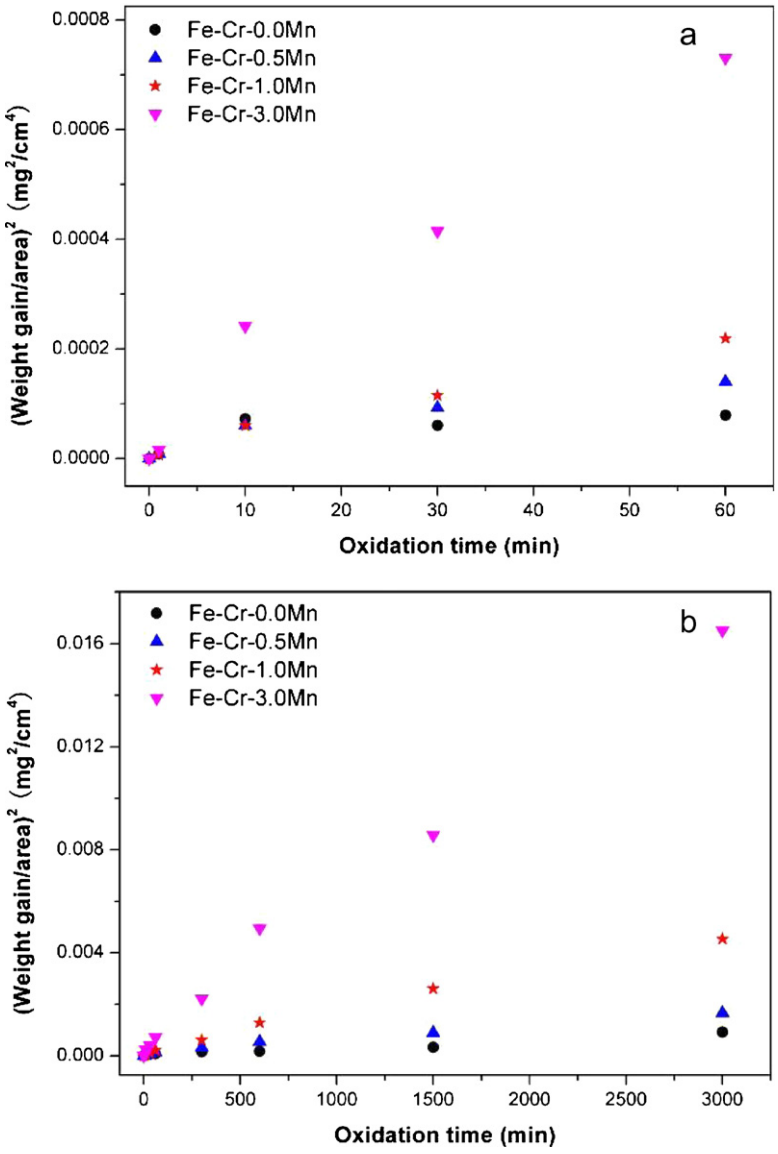

Fig. 3. Oxidation kinetics of the Fe–Cr–*x*Mn alloys oxidized at 750 °C in air within (a) 60 min and (b) 50 h.

from room temperature to 750 °C in the furnace within 20 min. Different coupons were taken out after designed oxidation time. The weight of all the coupons before and after oxidation was measured and recorded for calculating the weight gain upon oxidation by using a Sartorius BT-25S electronic balance with an accuracy of 10^{-5} g. The oxidation kinetics was obtained by plotting the weight gain against oxidation time.

The phase structure of the thermally grown oxide scale was characterized using an X-ray diffractometer (XRD, PANalytical X'Pert PRO) with Cu Kα radiation under conditions of 40 kV and 40 mA. Due to the detection limit of the θ–2θ mode, the θ–θ mode with an incident angle of 0.8° was employed to identify the phases of initially grown oxides. The microstructure and/or composition of the oxidized surface and/or cross-section of the coupons were examined by an environmental scanning electron microscope (ESEM, FEI Quanta 200) and a field emission scanning electron microscope (FSEM, FEI Sirion 200) with an energy dispersive spectroscope (EDS). X-ray photoelectron spectroscopy (XPS, VG Multilab 2000, Thermo Electron Corporation) and atom force microscope (AFM, SPA 400) were employed to determine the morphology and composition of the initially grown surface oxides. The electrical property of the oxidized samples was measured using the standard four-probe dc technique with a constant current density of 200 mA cm^{-2} at temperatures between 600 and 800 °C in air.

3. Results and discussions

3.1. Initial oxidation of Fe–Cr–xMn alloys

3.1.1. Oxide phases and oxidation kinetics

Fig. 2 is the XRD patterns of Fe–Cr–*x*Mn alloys oxidized at 750 °C in air for up to 50 h. Single oxide phase of Cr_2O_3 was obtained in the Fe–Cr–0.0Mn alloy oxidized within 50 h (Fig. 2a), which indicates that the residual Mn (<0.1 wt.%) in Fe–Cr alloy does not promote the formation of spinel type oxide. With Mn content increased in the alloy to 0.5 wt.%, only Cr_2O_3 type oxide formed within initial 30 min of oxidation, followed by gradually enhanced formation of $(Mn, Cr)_3O_4$ spinel oxide (Fig. 2b). As Mn content further increased in the alloy to 1 and 3 wt.%, formation of $(Mn, Cr)_3O_4$ spinel oxide started soon after 1 min oxidation (Fig. 2c and d); and Mn-rich oxide Mn_2O_3 appeared in the oxide scale after 5 h oxidation. The thickened Mn_2O_3 layer on top of the scale made invisible the diffraction

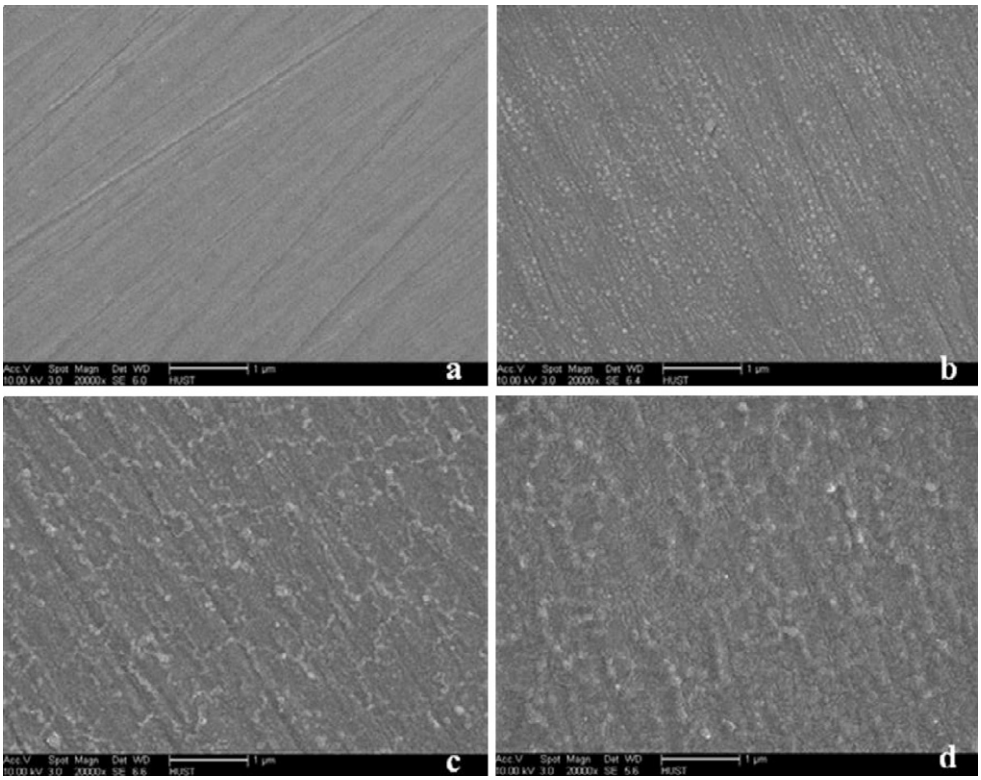

Fig. 4. SEM surface morphology of the Fe–Cr–0.0Mn alloy oxidized at 750 °C in air for (a) 30 s; (b) 60 s; (c) 5 min and (d) 10 min.

signals from the underneath Cr_2O_3 and $(Mn, Cr)_3O_4$ oxides in the θ–θ diffraction mode. Based on the XRD result, it can be seen that with extremely low Mn content in the Fe–Cr alloy, corundum type oxide is the only form of oxidation product within 50 h at 750 °C in air; with Mn content increased from 0.5 to 3 wt.%, the incubation time for formation of the spinel type oxide is shortened significantly to the level of 1 min, and more Mn-rich phase Mn_2O_3 type oxide is presented in the Fe–Cr alloy containing 3.0 wt.% of Mn.

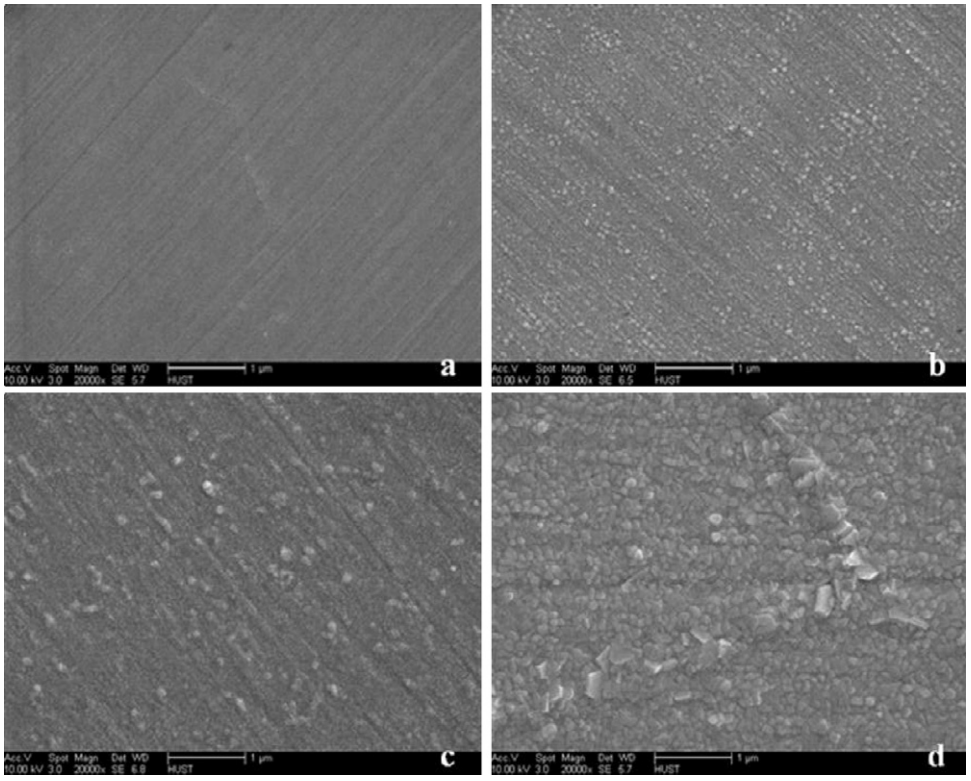

Fig. 5. SEM surface morphology of the Fe–Cr–0.5Mn alloy oxidized at 750 °C in air for (a) 30 s; (b) 60 s; (c) 5 min and (d) 10 min.

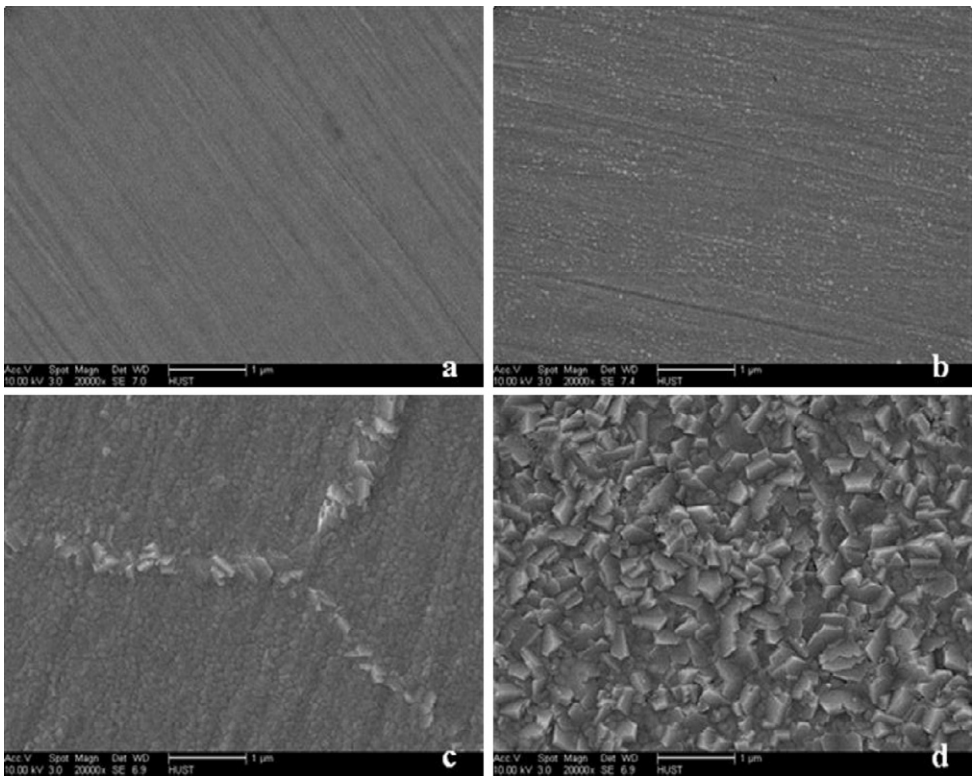

Fig. 6. SEM surface morphology of the Fe–Cr–1.0Mn alloy oxidized at 750 °C in air for (a) 30 s; (b) 60 s; (c) 5 min and (d) 10 min.

Fig. 3 shows the oxidation kinetics, the square of the area specific weight gain against the oxidation time, of the Fe–Cr–*x*Mn alloys oxidized at 750 °C in air. For oxidation within 2 min, the weight gain of all Fe–Cr–*x*Mn alloys is on the same level, regardless of Mn content, as seen in Fig. 3a. As the oxidation time prolonged, the oxidation rate of the Fe–Cr–3.0Mn alloy beyond 10 min is significant higher than those of the others. The general trend is that the oxidation rate increases with Mn content in the alloy, which becomes

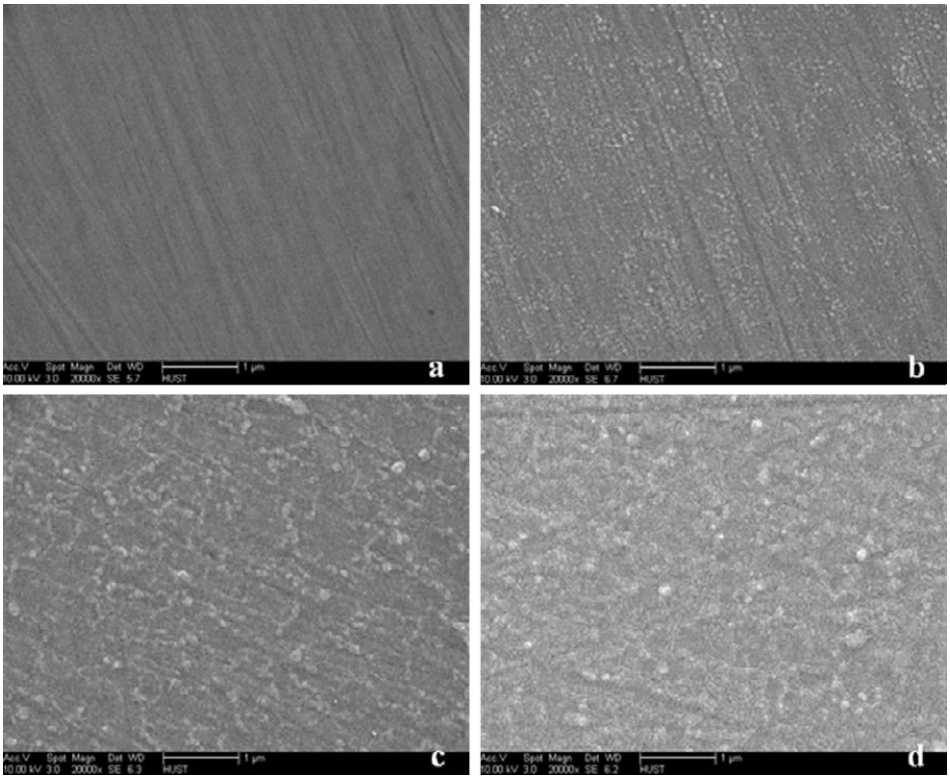

Fig. 7. SEM surface morphology of the Fe–Cr–3.0Mn alloy oxidized at 750 °C in air for (a) 30 s; (b) 60 s; (c) 5 min and (d) 10 min.

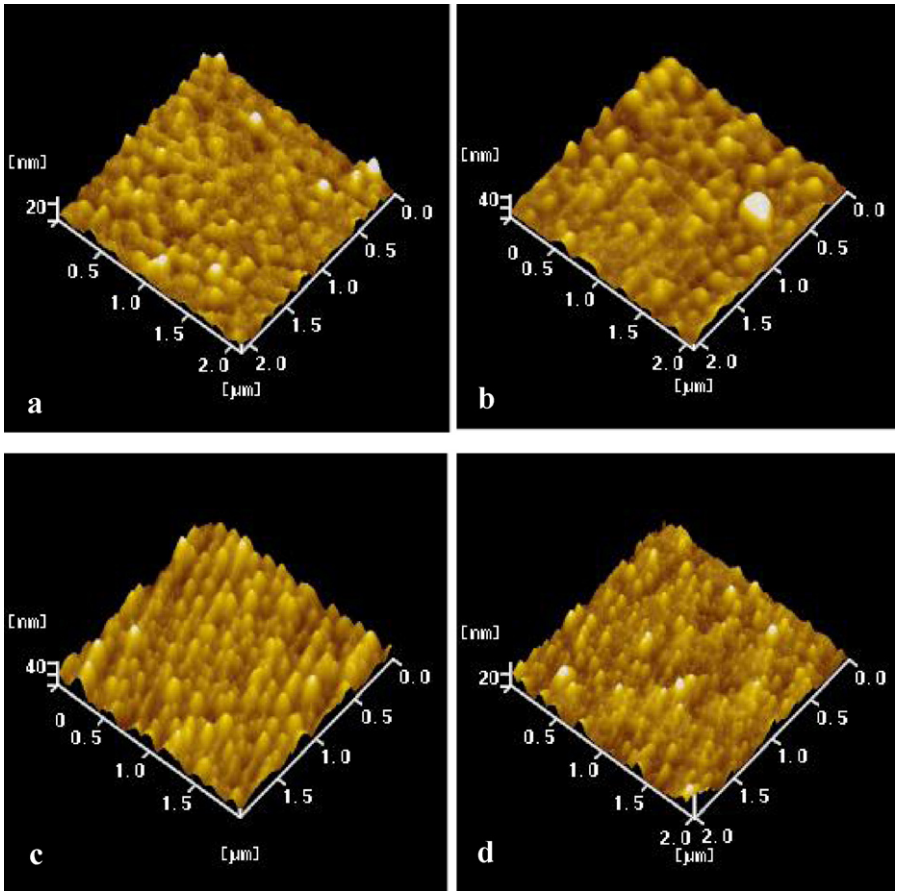

Fig. 8. AFM surface morphology of the Fe–Cr–*x*Mn alloys oxidized at 750 °C in air for 60 s: (a) 0.0Mn; (b) 0.5Mn; (c) 1.0Mn; (d) 3.0Mn.

more obvious with prolonged oxidation time in the alloys containing more than 0.5 wt.% of Mn (Fig. 3b). According to the XRD result above, it is confirmed that the increased oxidation rate of the alloys with Mn addition is associated with the formation of $(Mn, Cr)_3O_4$ and/or Mn_2O_3 phases in the oxide scale of the Fe–Cr alloys. The formation of $(Mn, Cr)_3O_4$ spinel and Mn_2O_3 phases in the oxide scale is expected to increase the electrical conductivity of the oxide scale and alleviate cathode Cr-poisoning [4,25–28]. However, excessive Mn content in the Fe–Cr alloy increase the oxidation rate; and consequently a much thicker oxide scale is formed, lowering the oxidation resistance of the alloy and increasing the electrical resistance of the oxide scale.

3.1.2. Morphology and composition of oxide scale

The surface morphology of the Fe–Cr–*x*Mn alloys initially oxidized for up to 10 min at 750 °C in air is shown in Figs. 4–7. The surface of the Fe–Cr–*x*Mn alloy after 30 s oxidation is clean under the resolution of the FSEM used; no oxides are observed other than the polishing scratches (Figs. 4a–7a). When oxidation time reaches 1 min, the surface of the Fe–Cr–*x*Mn alloys is decorated by uniformly distributed small oxide particles (Figs. 4b–7b). With increasing oxidation time to 5 min, the oxidized surfaces are fully covered by densely packed oxide particles (Figs. 4c and 7c), which are well grown with prism-like large oxides along the original grain boundary in the Fe–Cr–1.0Mn alloy. At 10 min of oxidation, the morphology of the oxidized surfaces of the Fe–Cr–0.0Mn and Fe–Cr–3.0Mn alloys are not changed significantly compared to those oxidized for 5 min (Figs. 4d and 7d); however, the surface oxide morphology of the Fe–Cr–0.5Mn and Fe–Cr–1.0Mn alloys is different from those oxidized for 5 min (Figs. 5d and 6d). It is noticed that the surface oxide morphology of the Fe–Cr–0.5Mn alloy oxidized for 10 min is similar to that of the Fe–Cr–1.0Mn alloy oxidized for 5 min; and the oxides on the surface of the Fe–Cr–1.0Mn alloy oxidized for 10 min (Fig. 6d) are well crystallized in prism shape on the outmost surface. According to the crystal structure of corundum and spinel oxides and the XRD result, it can be determined that the prisms are $(Mn, Cr)_3O_4$ spinel. The diffusion rate of ions along with the grain boundary is orders of magnitude faster than that of bulk diffusion [29–31], which explains the appearance of the large grain boundary oxides. From the fact that the grain boundary spinel oxides appeared earlier in the Fe–Cr–1.0Mn alloy than in the Fe–Cr–0.5Mn alloy, it is suggested that increasing Mn content in the Fe–Cr–*x*Mn alloys enhances the outward diffusion of Mn ions, shortening the oxidation time for initial formation of the spinel. The reason for the similarity of the surface oxide morphology in the Fe–Cr–0.0Mn and Fe–Cr–3.0Mn alloys may be that the surface oxide in both alloys is corundum type oxide, i.e., Cr_2O_3 and Mn_2O_3, respectively.

Fig. 8 is the AFM micrographs of surface oxide of the Fe–Cr–*x*Mn alloys initially oxidized for 60 s at 750 °C in air, showing similar morphology for all the oxidized surfaces, even though the oxide particles formed in the Fe–Cr–1.0Mn and Fe–Cr–3.0Mn alloys seem finer. Fig. 9 is the XPS surface analysis results of the Fe–Cr–*x*Mn alloys initially oxidized at 750 °C in air for 60 s, showing that Cr is the predominant element in the surface oxide of all the Fe–Cr–*x*Mn alloys and only insignificant amount of Mn is contained in that of the Fe–Cr–1.0Mn and Fe–Cr–3.0Mn alloys. This AFM observation result and XPS analysis are consistent to the above FSEM examinations and XRD patterns, once again confirming that the early oxidation is independent of the Mn content in the alloys and forms corundum type oxide. Thus, it can be concluded that Cr in the alloys is preferentially oxidized to form a protective layer of corundum

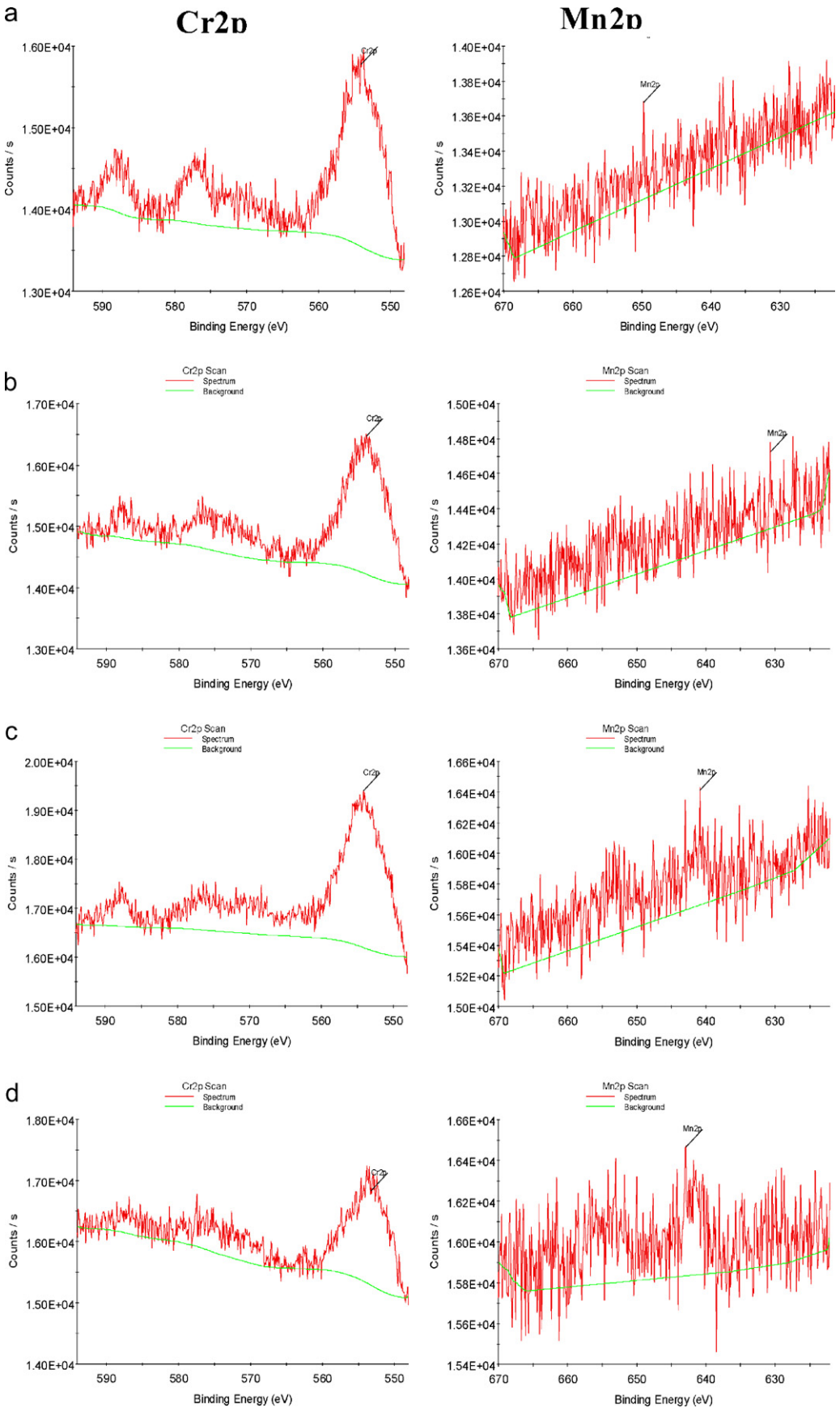

Fig. 9. XPS results of the Fe–Cr–*x*Mn alloys initially oxidized at 750 °C in air for 60 s: (a) 0.0Mn; (b) 0.5Mn; (c) 1.0Mn; (d) 3.0Mn.

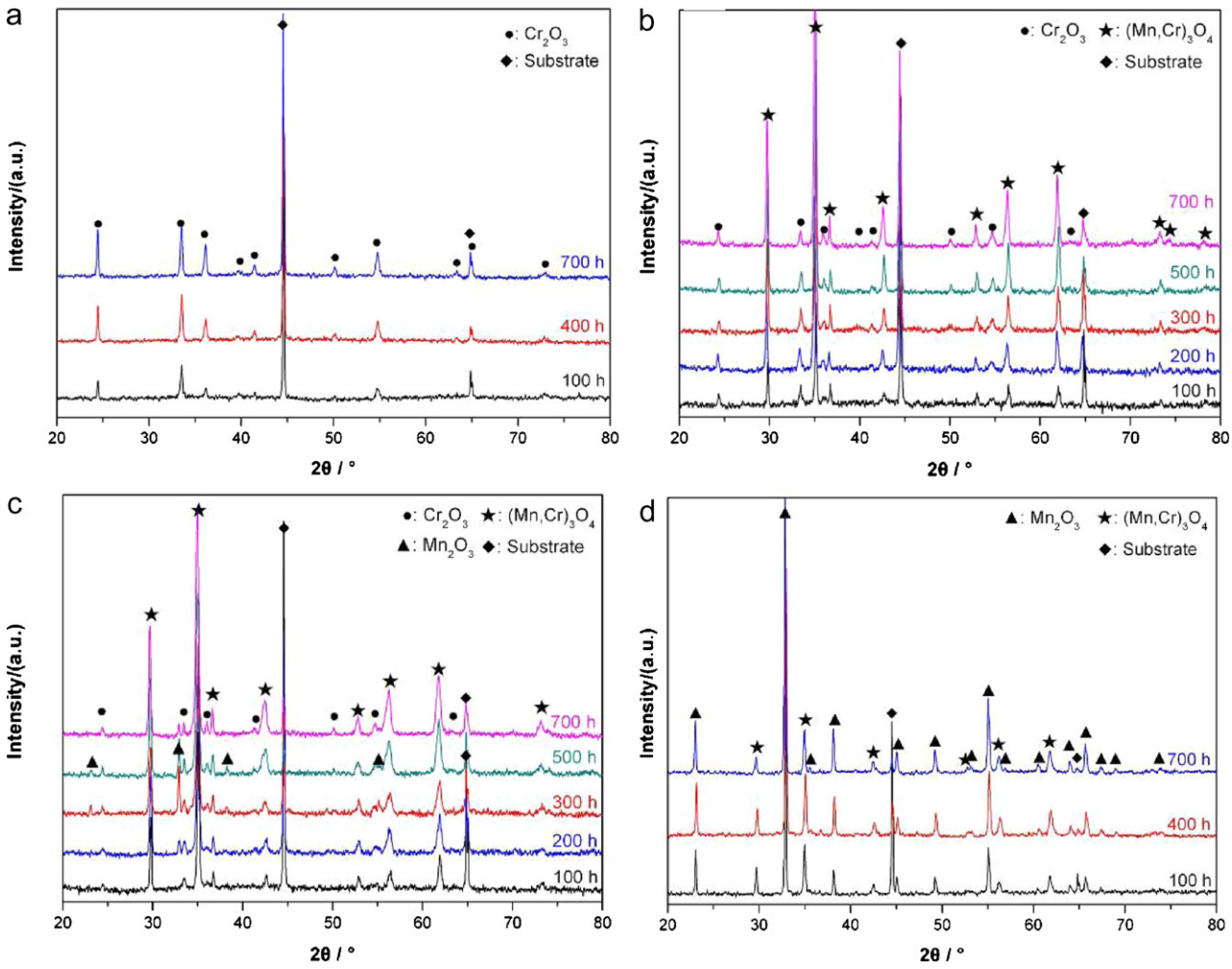

Fig. 10. XRD patterns of the Fe–Cr–*x*Mn alloys oxidized at 750 °C in air for up to 700 h: (a) 0.0Mn; (b) 0.5Mn; (c) 1.0Mn; (d) 3.0Mn.

type oxide during the early stage of oxidation; and subsequent oxidation of the alloys is accelerated due to the presence of Mn via its fast outward diffusion across the corundum oxide layer to form (Cr, Mn)$_3$O$_4$ or Mn_2O_3 on the top surface of the oxide scale.

3.2. Long-term oxidation of Fe–Cr–xMn alloys

3.2.1. Oxide phases and oxidation kinetics

Fig. 10 is the θ–2θ mode XRD patterns of Fe–Cr–*x*Mn (x = 0.0, 0.5, 1.0 and 3.0 wt.%) alloys oxidized at 750 °C in air for up to 700 h. The phases in the oxide scale of each alloy are basically the same as those oxidized for 50 h under the same conditions. Cr_2O_3 is the only phase in the oxide scale of the Fe–Cr–0.0Mn alloy oxidized for up to 700 h. With relatively low Mn content in the Fe–Cr–0.5Mn alloy, the oxide scale formed during 700 h of oxidation contains Cr_2O_3 and (Mn, Cr)$_3$O$_4$ phases. And in the Fe–Cr–1.0Mn and Fe–Cr–3.0Mn alloys, Mn-rich Mn_2O_3 phase forms with oxidation time, besides of Cr_2O_3 and (Mn, Cr)$_3$O$_4$.

Fig. 11 presents the oxidation kinetics of the Fe–Cr–*x*Mn (x = 0.0, 0.5, 1.0 and 3.0 wt.%) alloys oxidized at 750 °C in air for up to 700 h. As expected, in all cases, the square of specific area weight gain caused by oxidation increases linearly with the oxidation time, satisfying the diffusion-controlled parabolic law as described by:

$$\left(\frac{\Delta W}{A}\right)^2 = k_p t \quad (1)$$

where ΔW is the sample weight gain, A is the sample surface area, t is the oxidation time, and k_p (g^2 cm^{-4} s^{-1}), the parabolic rate constant, is the slope of the straight line in Fig. 11 and a measure of oxidation resistance. The experimentally obtained k_p for the Fe–Cr–*x*Mn alloys is listed in Table 2, which is in the order of 10^{-13} to 10^{-15} g^2 cm^{-4} s^{-1}. It is observed that the oxidation rate of the Fe–Cr–*x*Mn alloys increases with increasing the

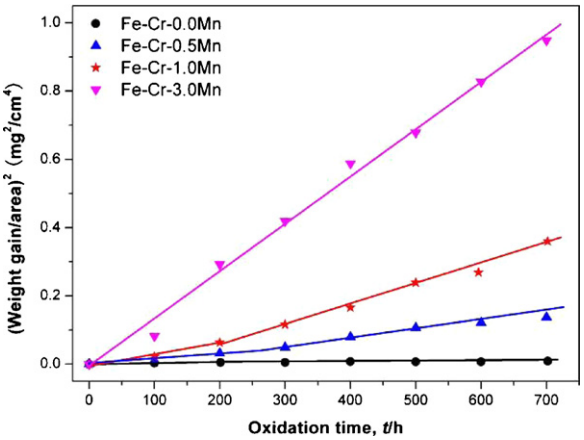

Fig. 11. Oxidation kinetics of the Fe–Cr–*x*Mn alloys oxidized at 750 °C in air for up to 700 h.

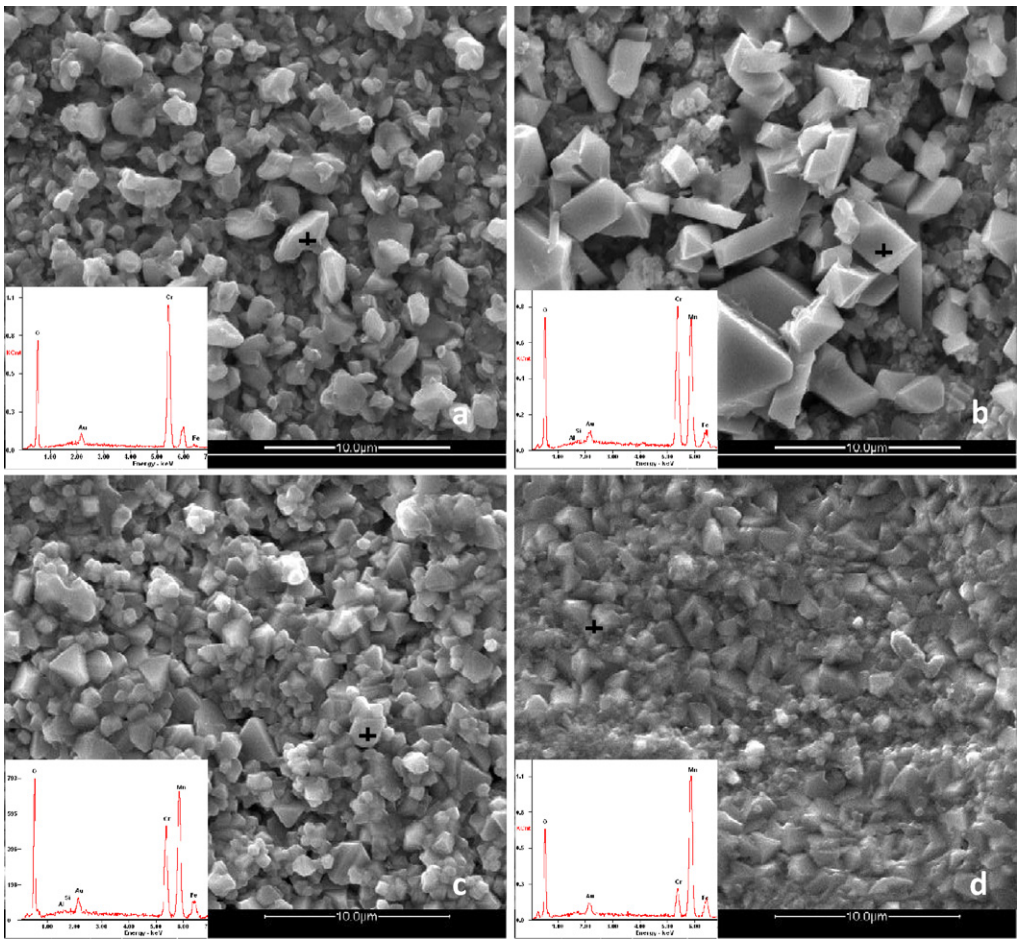

Fig. 12. SEM surface morphology, with inserted EDS analysis at the marked spot, of the Fe–Cr–*x*Mn alloys oxidized at 750 °C in air for 700 h: (a) 0.0Mn; (b) 0.5Mn; (c) 1.0Mn; (d) 3.0Mn.

Mn content, which indicates that it is the Mn containing in the alloys that accelerates the oxidation rate and affects the oxidation behavior of the Fe–Cr alloy. The k_p of the Fe–Cr–0.0Mn alloy is 3.8×10^{-15} g^2 cm^{-4} s^{-1}, which is the lowest among the alloys and two orders of magnitude lower than that of the Fe–Cr–3.0Mn alloy (3.8×10^{-13} g^2 cm^{-4} s^{-1}). Furthermore, no obvious change in oxidation rate during the 700 h oxidation was observed with the Fe–Cr–0.0Mn and Fe–Cr–3.0Mn alloys, instead, the Fe–Cr–0.5Mn and Fe–Cr–1.0Mn alloys experienced an initial slow oxidation with a lower rate constant, followed by a faster steady oxidation at a higher rate. The oxidation rate change occurred after 200 h oxidation and demonstrated a two-stage oxidation characteristic with two different slopes in the kinetics curves. Such multi-stage oxidation kinetics was observed previously in Fe–Cr and Ni–Cr alloys containing less than 1.0 wt.% of Mn [16,17], and was attributed to the formation of $MnCr_2O_4$ spinel. According to the XRD intensity change of $(Mn, Cr)_3O_4$ and Mn_2O_3 phases with oxidation time in Fig. 10b and c, it is expected that the oxidation rate change happened here in the Fe–Cr–0.5Mn and Fe–Cr–1.0Mn alloys is corresponded, respectively, to the enhanced formation of $(Mn, Cr)_3O_4$ in the Fe–Cr–0.5Mn alloy and Mn_2O_3 in the Fe–Cr–1.0Mn alloy. In the cases of Fe–Cr–0.0Mn and Fe–Cr–3.0Mn alloys, the oxidation was controlled by Cr and Mn outward diffusion, respectively, from the very beginning without rate-controlling mechanism change with oxidation time; therefore, a constant oxidation rate during the 700 h oxidation process is maintained.

Table 2
Parabolic rate constant (k_p) of the Fe–Cr–*x*Mn alloys oxidized at 750 °C in air.

Alloy	k_p (g^2 cm^{-4} s^{-1})
Fe–Cr–0.0Mn	3.8×10^{-15} (0–700 h)
Fe–Cr–0.5Mn	3.7×10^{-14} (0–250 h); 7.9×10^{-14} (250–700 h)
Fe–Cr–1.0Mn	8.8×10^{-14} (0–200 h); 1.7×10^{-13} (200–700 h)
Fe–Cr–3.0Mn	3.8×10^{-13} (0–700 h)

3.2.2. Morphology and composition of oxide scale

The surface morphology of the oxide scale of the Fe–Cr–*x*Mn alloys oxidized at 750 °C in air for 700 h is demonstrated in Fig. 12, with inserted EDS compositional analysis at the marked point. It can be seen that the Mn content in the surface oxide increases as the Mn content increases in the alloy from 0.0 to 3.0 wt.%, which is consistent with the result of XRD shown in Fig. 10 and confirms that Cr_2O_3 is the only oxide phase in the oxidized Fe–Cr–0.0Mn alloy and $(Mn, Cr)_3O_4$ and/or Mn_2O_3 formed in the alloys containing 0.5, 1.0 and 3.0 wt.% of Mn. This result suggests that higher Mn content in an alloy favors the formation of a Mn-rich surface oxide upon a long term oxidation due to fast diffusion of Mn ions across the scale. Fig. 13 presents the cross-section of oxide scales formed in the Fe–Cr–*x*Mn alloys oxidized for 700 h in air. The thickness of the oxide scale increases from 1 to 7 μm as the Mn content in the alloy changes from 0.0 to 3.0 wt.%, which is in agreement with the oxidation kinetics shown in Fig. 11 and suggests that addition of Mn in the Fe–Cr alloy decreases its oxidation resistance at 750 °C in air. A dense layer of Cr_2O_3 can prevent further oxidation of the substrate of the Mn free Fe–Cr alloy; however, with the addition of Mn into the Fe–Cr alloy, the fast outward diffusion of Mn ions leads

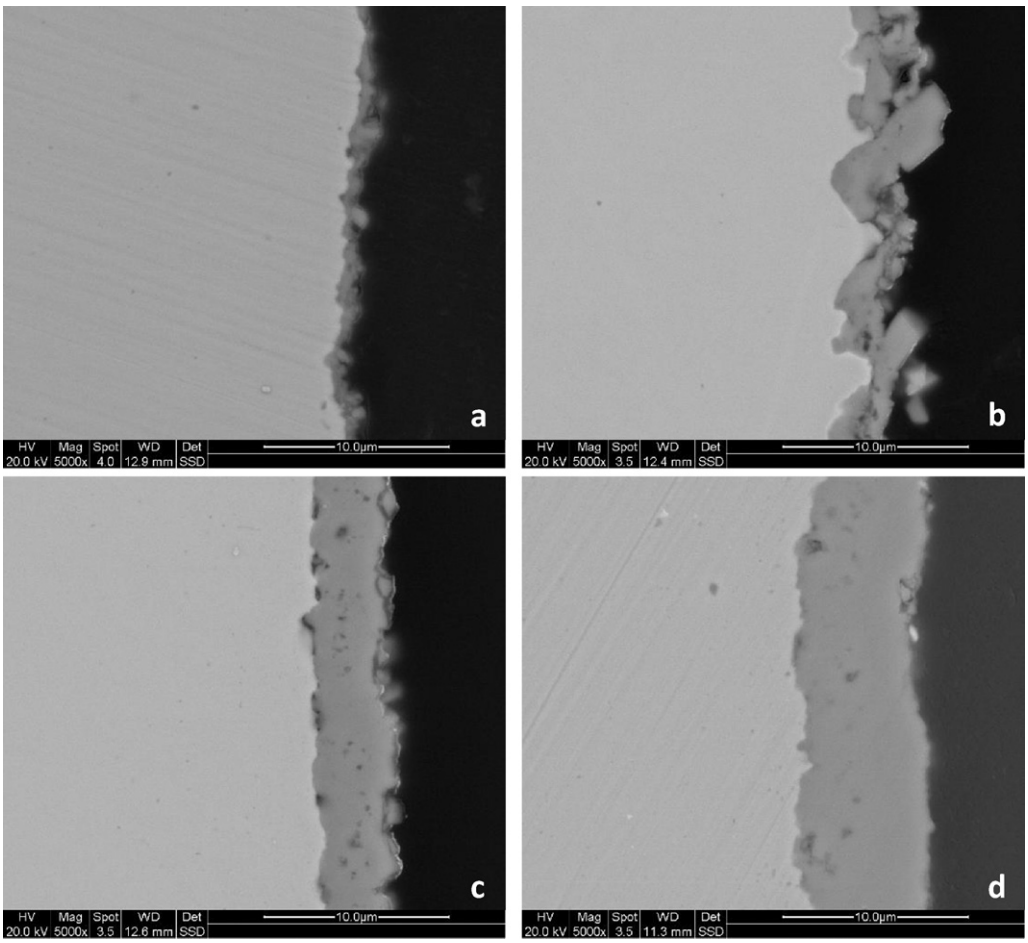

Fig. 13. SEM cross-sectional morphology of the Fe–Cr–*x*Mn alloys oxidized at 750 °C in air for 700 h: (a) 0.0Mn; (b) 0.5Mn; (c) 1.0Mn; (d) 3.0Mn.

to an accelerated oxidation. Fig. 14 is the results of compositional analysis made by EDS line scan across the oxide scale shown in Fig. 13. In consideration with the above XRD results and the cross-sectional morphology of the oxide scale, the profiles indicate that only a layer Cr_2O_3 formed on the surface of the Fe–Cr–0.0Mn alloy; a duplex oxide scale formed on the surface of the Fe–Cr–0.5Mn alloy with $(Mn, Cr)_3O_4$ on top of Cr_2O_3; triple layered oxide scale formed on the surface of the Fe–Cr–1.0Mn alloy with $(Mn, Cr)_3O_4$ between the inner Cr_2O_3 and outer Mn_2O_3; and a double layered oxide scale formed on the surface of the Fe–Cr–3.0Mn alloy with Mn_2O_3 on top of $(Mn, Cr)_3O_4$.

3.2.3. Electrical conductivity of oxide scale

The oxidation of metallic interconnect is inevitable in SOFC operating environment, and the thermally grown oxides with semi-conductor behavior will significantly deteriorate the cell performance after long term oxidation. A low and stable electrical resistance is required for metallic alloys as the interconnects of SOFCs. The electrical resistance of the substrate alloy is negligible as it is insignificant compared with the formed oxide scale, and the main contribution to the electrical resistance of the metallic interconnect comes from the thermally grown oxide scale. The area specific resistance (ASR, $\Omega\,cm^2$), which measures both the electrical conductivity and thickness of the formed oxide scale, is usually adopted in selecting metallic alloys for the interconnects. Fig. 15 shows the measured ASR of the Fe–Cr–*x*Mn alloys oxidized at 750 °C in air for 700 h as a function of measurement temperature *T*. It is noticed that the ASR increases as the measurement temperature decreases, and log(ASR/*T*) is linearly proportional to 1/*T* approximately with a slight change in slope at around 700 °C, showing the electrical characteristic of semi-conductors as described by the Arrhenius equation:

$$\frac{\mathrm{ASR}}{T} = A\,\exp\left(\frac{E_a}{kT}\right) \tag{2}$$

where *A* is a pre-exponential constant, *T* the absolute temperature, E_a the activation energy, and *k* the Boltzmann's constant. The obtained activation energy is in the range from 0.37 to 0.43 eV and from 0.26 to 0.29 eV for temperatures above and below 700 °C, respectively, which is somewhat lower than those obtained in the same temperature range for SUS 430 alloy oxidized at 750 °C for 400 h [32]. As a matter of fact, such slope change was also observed in oxidized Ni-based alloys [33–35], possibly due to the transition of diffusion from the intrinsic to the extrinsic charge carriers [36]. And the ASR increases with Mn content in the alloy at the temperatures in the range of measurement, corresponding to the oxidation rate and oxide scale thickness of the alloy. In fact, the formation of more conductive $(Mn, Cr)_3O_4$ spinel and Mn_2O_3 with Mn addition in the alloy improves the electrical conductivity of the formed oxide scale [1,4,26–28]; however, it is the excessively thicker oxide scale formed in the Mn containing alloys that increases the electrical resistance of the scale. This result makes it clear that the balance of oxide conductivity and thickness is of importance for the alloy subjected to the application of the metallic interconnects in SOFCs. For the purpose of lowering the electrical resistance of the oxide scale formed, Mn free Fe–17Cr alloy for the interconnect application is suggested. In order to alleviate the cathode Cr-poisoning caused by Cr evaporation from Cr_2O_3 during SOFC operation, Cr-free coatings,

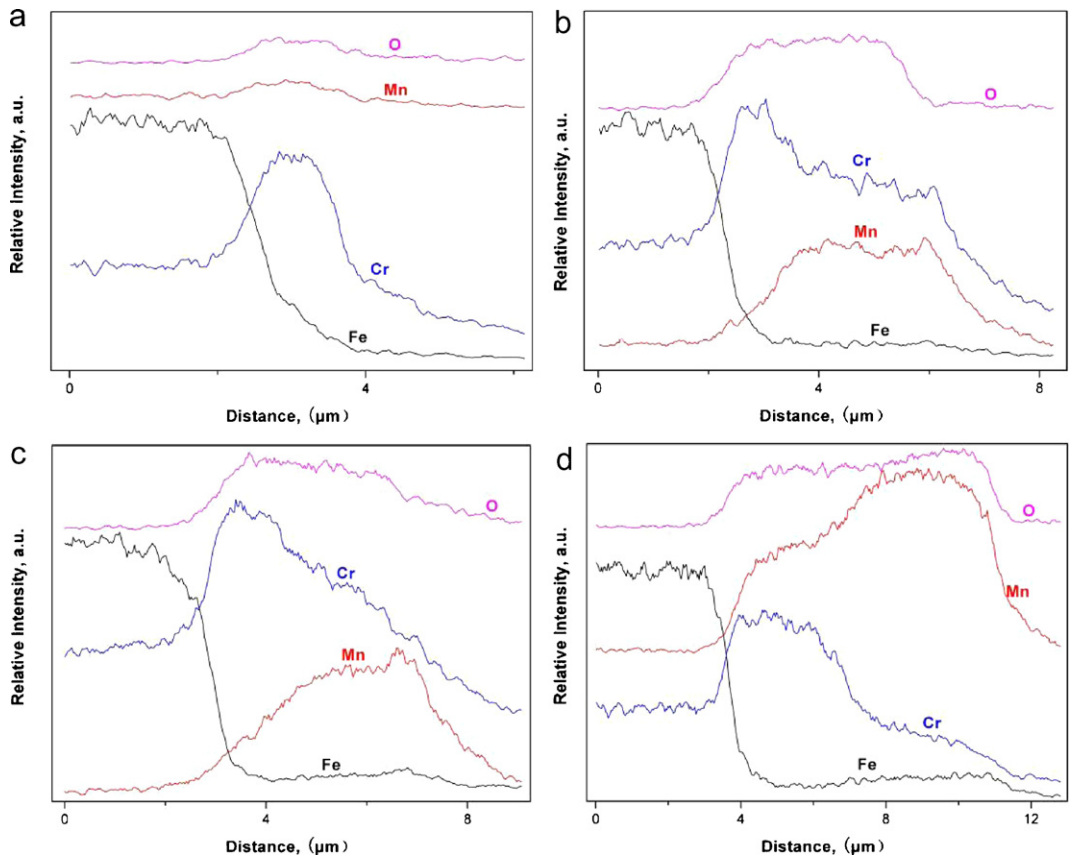

Fig. 14. Compositional profile of EDS line scan of cross-sectioned Fe–Cr–*x*Mn alloys oxidized at 750 °C in air for 700 h: (a) 0.0Mn; (b) 0.5Mn; (c) 1.0Mn; (d) 3.0Mn.

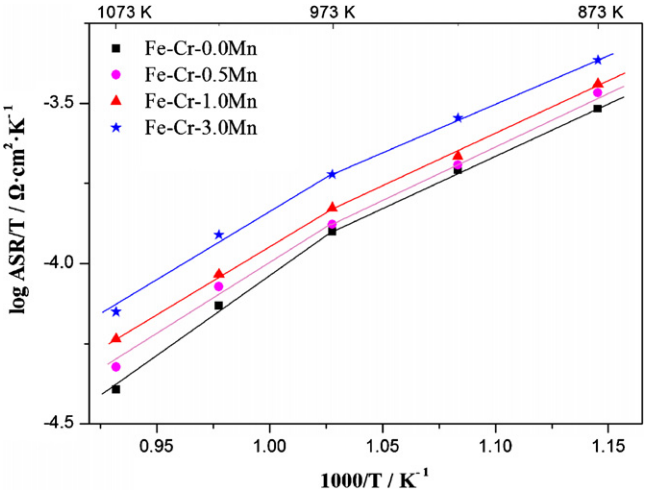

Fig. 15. Dependence of the ASR on temperature for the Fe–Cr–*x*Mn alloys oxidized at 750 °C in air for 700 h.

such as Mn–Co [37,38] and Ni–Mn [39] spinels, are recommended to be applied on the Mn free Fe–17Cr alloy.

4. Conclusions

The basic conclusions forthcoming from present work can be made as follows:

(1) The CTE of the Fe–Cr–*x*Mn alloys (x = 0.0, 0.5, 1.0 and 3.0 wt.%) is in the range of 12.5–13.0 × 10^{-6} K^{-1} between 35 and 800 °C, which is well matched to that of SOFC cell components (typically 10–13 × 10^{-6} K^{-1}).

(2) At the initial stage of oxidation within 1 min at 750 °C in air, Cr is preferentially oxidized to form Cr_2O_3 protective layer, which is slightly doped by Mn in the Fe–Cr–1.0Mn and Fe–Cr–3.0Mn alloys. The oxidation rate and surface oxide morphology are similar to each other for all the Fe–Cr–*x*Mn alloys.

(3) Oxidation rate of the Fe–Cr–*x*Mn alloys increases subsequently with the content of Mn in the alloy due to fast outward diffusion of Mn across the initially formed corundum type oxide layer to form Mn-rich oxides, such as $(Mn, Cr)_3O_4$ and Mn_2O_3 on the top, resulting in a multi-layered oxide scale, which corresponds to a multi-stage oxidation kinetics in the alloys containing 0.5 and 1.0 wt.% of Mn.

(4) The ASR of the oxide scale increases with the Mn content in the alloy due to a thicker oxide scale formed at a higher oxidation rate, even though the electrical conductivity of the Mn-rich phases $(Mn, Cr)_3O_4$ and Mn_2O_3 are lower than that of the corundum type oxide.

(5) Mn-free Fe–17Cr alloy is preferred as the material for metallic interconnects of SOFCs in terms of the oxidation behavior and electrical conductivity. In order to alleviate the cathode Cr-poisoning caused by Cr evaporation from Cr_2O_3 during SOFC operation, Cr-free coatings, such as Mn–Co and Ni–Mn spinels, are recommended.

Acknowledgments

This research was financially supported by National Natural Science Foundation of China (No. 50771048), Provincial Natural Science Foundation of Hubei (2008CDA004) and Fundamental Research Funds for the Central Universities (HUST2010ZD012). The

SEM and XRD work were conducted at the Analytical and Testing Center of Huazhong University of Science and Technology.

References

[1] W.Z. Zhu, S.C. Deevi, Mater. Res. Bull. 38 (2003) 957–972.
[2] Z.G. Yang, Int. Mater. Rev. 53 (2008) 39–54.
[3] N. Shaigan, W. Qu, D.G. Ivey, W. Chen, J. Power Sources 195 (2010) 1529–1542.
[4] S.J. Geng, J.H. Zhu, J. Power Sources 160 (2006) 1009–1016.
[5] J. Rufner, P. Gannon, P. White, M. Deibert, S. Teintze, R. Smith, H. Chen, Int. J. Hydrogen Energy 33 (2008) 1392–1398.
[6] J. Froitzheim, G.H. Meier, L. Niewolak, P.J. Ennis, H. Hattendorf, L. Singheiser, W.J. Quadakkers, J. Power Sources 178 (2008) 163–173.
[7] B. Hua, J. Pu, F.S. Lu, J.F. Zhang, B. Chi, J. Li, J. Power Sources 195 (2010) 2782–2788.
[8] W.Z. Zhu, S.C. Deevi, Mater. Sci. Eng. A 348 (2003) 227–243.
[9] J.W. Fergus, Mater. Sci. Eng. A 397 (2005) 271–283.
[10] T. Horita, Y.P. Xiong, K. Yamaji, N. Sakai, H. Yokokawa, J. Electrochem. Soc. 150 (2003) A243–A248.
[11] Z.G. Yang, M.S. Walker, P. Singh, J.W. Stevenson, T. Norby, J. Electrochem. Soc. 151 (2004) B669–B678.
[12] S.P. Simner, M.D. Anderson, G. Xia, Z. Yang, L.R. Pederson, J.W. Stevenson, J. Electrochem. Soc. 152 (2005) A740–A745.
[13] Z. Yang, J.S. Hardy, M.S. Walker, G. Xia, S.P. Simner, J.W. Stevenson, J. Electrochem. Soc. 151 (2004) A1825–A1831.
[14] D.E. Alman, P.D. Jablonski, Int. J. Hydrogen Energy 32 (2007) 3743–3753.
[15] Z. Yang, G. Xia, X. Li, J.W. Stevenson, Int. J. Hydrogen Energy 32 (2007) 3648–3654.
[16] J. Pu, J. Li, B. Hua, G.Y. Xie, J. Power Sources 158 (2006) 354–360.
[17] J. Li, J. Pu, B. Hua, G.Y. Xie, J. Power Sources 159 (2006) 641–645.
[18] R.K. Wild, Corros. Sci. 17 (1977) 87–104.
[19] R.E. Lobnig, H.P. Schmidt, K. Hennesen, H.J. Grabke, Oxid. Met. 37 (1992) 81–93.
[20] M.G.C. Cox, B. McEnaney, V.D. Scott, Philos. Mag. 26 (1972) 839–851.
[21] F.H. Stott, F.I. Wei, C.A. Enahoro, Mater. Corros. 40 (1989) 198–205.
[22] A.L. Marasco, D.J. Young, Oxid. Met. 36 (1991) 157–174.
[23] I.G. Crouch, J.C. Scully, Oxid. Met. 15 (1981) 101–135.
[24] I. Saeki, H. Konno, R. Furuichi, Corros. Sci. 38 (1996) 1595–1612.
[25] M Stanislowski, E. Wessel, K. Hilpert, T. Markus, L. Singheiser, J. Electrochem. Soc. 154 (2007) A295–A306.
[26] N. Sakai, T. Horita, Y. Xiong, K. Yamaji, H. Kishimoto, M.E. Brito, H. Yokokawa, T. Maruyama, Solid State Ionics 176 (2005) 681–686.
[27] Z. Lu, J.H. Zhu, E.A. Payzant, M.P. Paranthaman, J. Am. Ceram. Soc. 88 (2005) 1050–1053.
[28] S.J. Geng, J.H. Zhu, Z.G. Lu, Scripta Mater. 55 (2006) 239–242.
[29] S. Matsunaga, T. Homma, Oxid. Met. 10 (1976) 361–376.
[30] H.V. Atkinson, Oxid. Met. 28 (1987) 353–389.
[31] P. Kofstad, K.P. Lillerud, Oxid. Met. 17 (1982) 177–194.
[32] B. Hua, J. Pu, J.F. Zhang, F.S. Lu, B. Chi, J. Li, Funct. Mater. 39 (2008) 1689–1693.
[33] B. Hua, J. Pu, J.F. Zhang, F.S. Lu, B. Chi, J. Li, J. Electrochem. Soc. 156 (2009) B93–B98.
[34] B. Hua, F.S. Lu, J.F. Zhang, Y.H. Kong, J. Pu, B. Chi, J. Li, J. Electrochem. Soc. 156 (2009) B1261–B1266.
[35] S.J. Geng, J.H. Zhu, Z.G. Lu, Electrochem. Solid-State Lett. 9 (2006) A211–A214.
[36] P. Shewmon, Diffusion in Solids, 2nd edition, The Minerals Metals & Materials Society, 1989, pp. 151–164.
[37] B. Hua, J. Pu, W. Gong, J.F. Zhang, F.S. Lu, J. Li, J. Power Sources 185 (2008) 419–422.
[38] B. Hua, Y.H. Kong, F.S. Lu, J.F. Zhang, J. Pu, J. Li, Chin. Sci. Bull. 55 (2010) 3831–3837.
[39] W.Y. Zhang, J. Pu, B. Chi, J. Li, J. Power Sources 196 (2011) 5591–5594.